

## 3D printing lunar architecture with a novel cable-driven printer

Dianjin Zhang, Dekai Zhou <sup>\*\*</sup>, Guangyu Zhang, Guangbin Shao, Longqiu Li <sup>\*</sup>

State Key Laboratory of Robotics and System, Harbin Institute of Technology, Harbin, 150001, China



### ARTICLE INFO

**Keywords:**

Lunar architecture  
 Cable-driven printer  
 Small weight  
 Reconstruction

### ABSTRACT

Considerable attention has been paid to the exploration of moon, especially the construction of lunar habitat. However, few studies are found working on the construction equipment being suitable for trans planetary transportation, assembly, and working in lunar environment. This paper proposed a novel cable-driven printer used to build lunar architecture. The pose measurement and control strategy of the printing system is proposed. To study the reconfiguration characteristic of the cable-driven printer, several trees with arbitrary locations were selected as the rack to reconstruct the system outdoors. The key factors such as the sensitivity of pose deviation to system parameters affecting the reconstruction performance is discussed. The forming space of the cable-driven printer is analyzed theoretically and the forming ability of the system is verified experimentally. It is found that the cable-driven printer has the advantages of simple structure, small weight, large forming space and good reconfiguration characteristic, which shows the great potential of the proposed cable-driven printer in the construction of lunar architecture.

### 1. Introduction

In recent years, there has been an increasing interest in lunar exploration. One of the most essential task for lunar exploration is to build lunar habitat. Compared with building on earth, the construction of lunar architecture is full of challenges. These challenges mainly come from the harsh environment of the moon, such as extreme temperature, no atmosphere and strong radiation. On the other hand, there is no construction equipment and materials on the moon.

Considering the cost and difficulty of transportation, In Situ Resource Utilization (ISRU) is a relatively recognized construction method, in which lunar soil as a building material is advocated [1–5]. Several work can be found in literature on ISRU. Cesaretti et al. [6] produced a section of the outpost wall at full scale using D-shape printing technology. Considering the weight and volume of the printer and materials required, they estimate that it is difficult to transport the equipment and related materials to the moon.

Use of robot as a building printing device is another way to manufacture structure in space. Zhang et al. [7] proposed a 3D printing system using multiple mobile arm robots to simultaneously print a large single-piece structure. Zhou et al. [8] proposed an autonomous robot construction system for the lunar habitat. One of the advantages of using the arm loaded on the mobile platform to build the lunar base is that the

printer can be moved freely and flexibly on the ground. However, the construction height of the arm printer is very limited. Besides, due to the arm length limitation, it is difficult for the manipulator to construct an internal area structure for construction.

With the advantages of small weight and large forming space [9,10], cable-driven robots is an effective method to solve the conflict between trans planetary transportation and construction. Bosscher et al. [11] proposed a kind of architecture printing system consisting of a mobile contour crafting platform driven by a translational cable-suspended robot. To avoid the interference between cables and the building under construction, four independent vertical driven crossbars are added to the frame, which increases the complexity of the device and the difficulty of assembly, debugging, and control of the device. Barnett et al. [12] use a suspension foam printer to build a 2.16-m-high statue. The disadvantage of the cable-suspended robot is that the balance of the end nozzle depends on gravity. In addition, its anti-interference ability, motion, and dynamic performance will be poor under microgravity environment.

As can be seen, there is no suitable equipment for trans planetary transportation and lunar environment construction. The purpose of this study is to fill this research gap. We proposed a novel cable-driven printer which overcomes the problem that the cable of the mechanism is easy to interfere with the printed object. The pose control and printing

\* Corresponding author.

\*\* Corresponding author.

E-mail addresses: [dekaizhou1989@gmail.com](mailto:dekaizhou1989@gmail.com) (D. Zhou), [longqiuli@hit.edu.cn](mailto:longqiuli@hit.edu.cn) (L. Li).

ability of the cable-driven printer is studied in detail. Because reconstruction of the cable-driven printer is a problem that must be considered in the use of the printing system, we studied the reconstruction characteristic of the cable-driven printer. The experiments and simulation show that the proposed cable-driven printer is suitable for the construction of lunar architecture.

## 2. Design

The concept of building lunar architecture with the cable-driven printer is showed in Fig. 1. During transportation, the frame and mobile platform are composed of telescopic rods while the system can be compressed to a smaller volume. After being transported to the lunar surface, the frame is placed near the construction site. Then, the telescopic rods are extended, and the cables are tensioned while the frame is fixed. After that, the system starts to print lunar architecture as required. In order to complete these tasks, the key issue is to ensure that the printer is light in weight, easy to reconstruct, and great forming ability. This paper will elaborate on the research work around these problems.

Because the balance of the actuator depends on gravity, the suspension cable-driven robot has the disadvantages of poor motion performance and low stiffness. Especially in the low gravity environment of the moon, it is difficult to guarantee the accuracy of the printing trajectory as long as the suspension cable-driven printer is disturbed. The cable-driven robot with full or redundant constraints has good anti-interference ability, but as a 3D printer, it has the disadvantage of interference between the rope and the printed object, which greatly limits the forming space of the cable-driven printer. The relationship between the forming space and parameters of a two-dimensional cable-driven mechanism is showed in Fig. 2. In the figure,  $a_1$  and  $a_2$  represent the connection points between the cables and the frame,  $l_b$  is the height difference of the connection points between cables and the actuator,  $p$  is the point of intersection between the cables. The blue area is the maximum forming space where cables do not interfere with the printed object. As can be seen from the figure, with the increase of  $l_b$ , the forming space of the mechanism gradually increases, and  $p$  gradually approaches  $a_1$  and  $a_2$ . The mechanism in Fig. 2(d) is equivalent to the

mechanism with a very large  $l_b$ , that is, the distance between  $p$ ,  $a_1$  and  $a_2$  can be seen as 0 compared with  $l_b$ . At this time, the forming space of the cable-driven printer reaches the maximum, which is equivalent to the wrench-feasible workspace [13] of the printer.

By extending the mechanism in Fig. 2(d) from 2D to 3D, the novel cable-driven printer proposed in the paper is obtained. The cable-driven printer has 8 cables as shown in Fig. 3(a). The mechanism is mainly composed of a rack, winches, cables, and a mobile platform. The winches fixed points are located near the 4 upper vertices of a cube. The mobile platform consists of a rectangular plate and a rod perpendicular to the plate. All cables are located above the nozzle, effectively avoiding interference between cables and printed object. The cable-driven printer has redundant degrees of freedom, which ensures that the mechanism does not depend on gravity. It means that no matter what the gravity is, the mechanism can always keep the balance of the mobile platform by tensioning cables. This feature allows the system to better adapt to low gravity environments. To obtain more accurate pose of the nozzle and ensure that the cable tension is within the given range, the cable-driven printing system also includes eight tension sensors and a camera. Fig. 3(b) shows the developed cable-driven printing system. It should be noted that the complete framework of the prototype in Fig. 3(b) will not be sent to the lunar surface. What will eventually be sent to the moon is the frame composed of telescopic rods. The cube frame is built to facilitate the study of the forming space and forming capacity of the designed cable-driven system.

## 3. Methods

### 3.1. Measurement

Because of the coupling of the motion of the nozzle, it is a challenge to measure the pose of the nozzle of the cable-driven printer quickly and accurately. In this paper, Monocular Stereo Vision [14–16] is used to measure the pose of the mobile platform. Monocular Stereo Vision uses a model composed of geometric features to locate the target. Here, the geometric feature is an array of circles in a calibration disk. The circles are mapped to the ellipses in the image through the camera matrix. After

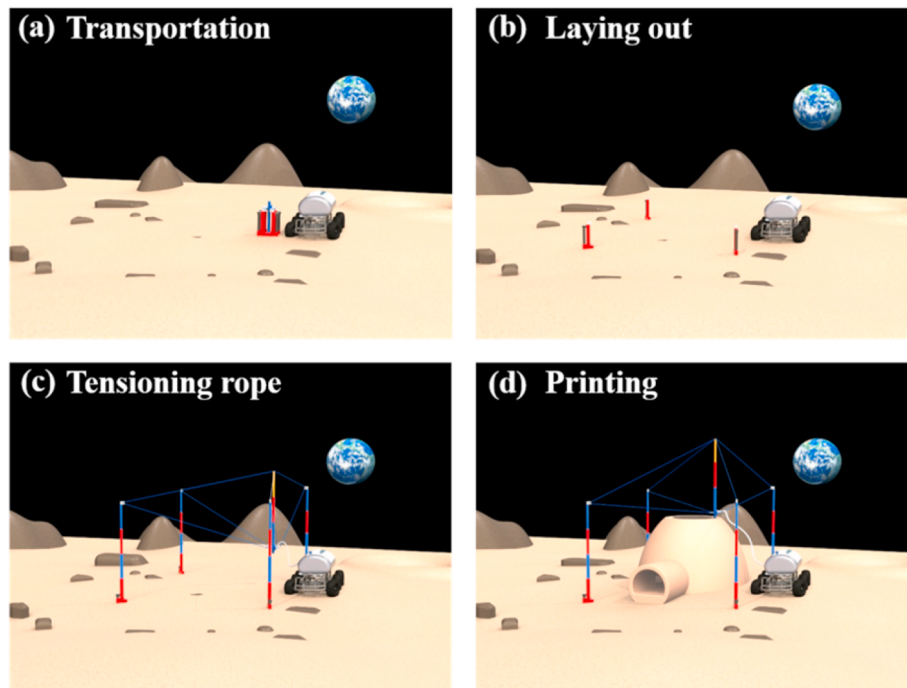


**Fig. 1.** The concept of building lunar architecture with the cable-driven printer. (a) The contracted system is transported to the surface of the moon. (b) The rack is placed near the construction site. (c) The frame is unfolded, and cables are tightened to form a printing system. (d) Printing the lunar architecture with the printer.

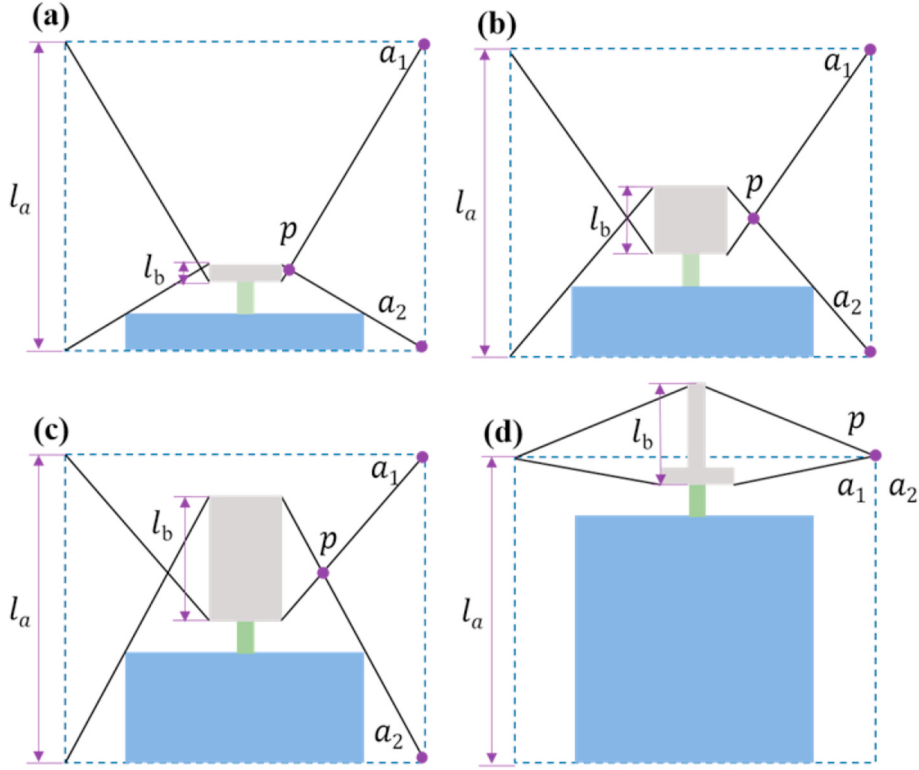


Fig. 2. The relationship between the forming space and parameters of cable-driven mechanism.

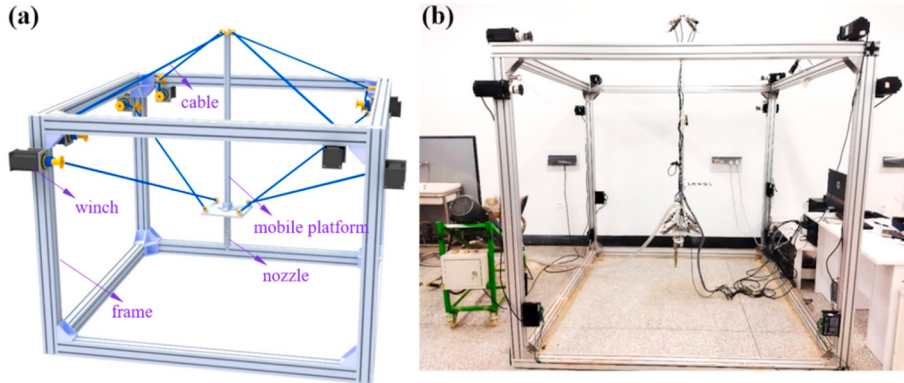


Fig. 3. The designed cable-driven printer. (a) The structure diagram of the proposed cable-driven printer. (b) The developed cable-driven printing system.

fitting the elliptic equation, the ellipse center is obtained. Through the method of Perspective-N-Point (PNP) [17], the external parameters of the camera can be obtained, that is, the pose of the camera relative to the calibration disk. As can be seen from Fig. 4, the calibration disk is fixed on the mobile platform, and then the pose of the mobile platform relative to the camera coordinate system can be obtained. Where  $P_{wc}$  is the homogeneous transformation matrix of the camera coordinate system  $\{C\}$  relative to the frame coordinate system  $\{W\}$ ;  $P_{co}$  is the homogeneous transformation matrix of the calibration disk coordinate system  $\{O\}$  relative to the camera coordinate system  $\{C\}$ ;  $P_{op}$  is the homogeneous transformation matrix of the mobile platform coordinate system  $\{P\}$  relative to the calibration disk coordinate system  $\{O\}$ . The homogeneous transformation matrix  $P_{wp}$  of the mobile platform coordinate system  $\{P\}$  relative to the frame coordinate system  $\{W\}$  is obtained from the following formula:

$$P_{wp} = P_{wc} P_{co} P_{op} \quad (1)$$

First, the calibration disk is placed at the origin of the frame. The pose of the camera relative to the calibration disk is measured. Then the homogeneous transformation matrix  $P_{cd}$  of the camera coordinate system relative to the calibration disk coordinate system is obtained.  $P_{dc}$  is the inverse of  $P_{cd}$ . In this process, it is considered that the calibration disk coordinate system coincides with the designed frame coordinate system, thus  $P_{wc} = P_{dc}$ . In the motion of the mobile platform, the pose of the calibration disk coordinate system relative to the camera coordinate system is measured, and the  $P_{co}$  is obtained. The calibration disk is fixed on the mobile platform, and its relative pose remains unchanged. That is,  $P_{op}$  is a given invariant homogeneous transformation matrix.

In the calculation of  $P_{wc}$ , the calibration disk cannot be accurately placed at the origin of the rack, which makes  $P_{wc}$  not equal to  $P_{dc}$ . However, the mechanism parameters used in calculating the length of the driving cable is relative to the frame coordinate system. The inconsistency of the coordinate system will cause the pose deviation of the mobile platform. One way to reduce the influence of the error source

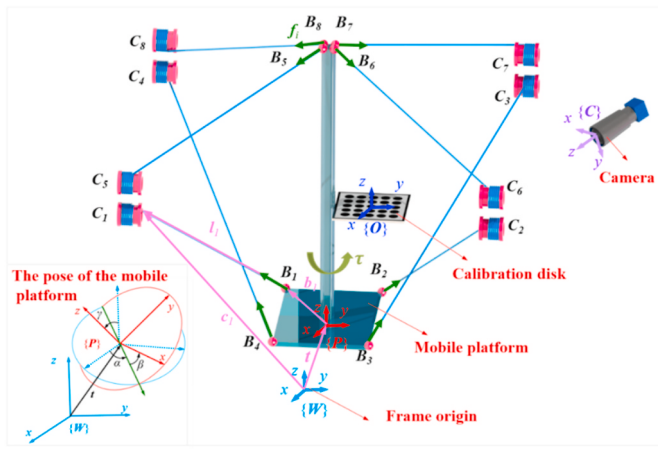


**Fig. 4.** Schematic diagram of the cable-driven printer. The purple line describes the kinematic vector loop of the system. The lower left corner describes the position and attitude of the moving platform. Four coordinate systems  $\{\mathbf{W}\}$ ,  $\{\mathbf{P}\}$ ,  $\{\mathbf{O}\}$  and  $\{\mathbf{C}\}$  are used to describe the visual measurement of the pose of the moving platform. (For interpretation of the references to color in this figure legend, the reader is referred to the Web version of this article.)

is to calibrate the mechanism parameters relative to the calibration disk coordinate system and use the calibration disk coordinate system as the new frame coordinate system. Another method is used in the experiment: using the measured pose and cable tension of the mobile platform as feedback information to adjust the driving cable length to reduce the pose error. This is described in detail in 3.2 Control.

### 3.2. Control

The dynamic model of the cable-driven printer includes mobile platform dynamics and cable dynamics. The mobile platform dynamics can be derived from Newton-Euler equation. It is considered that the tensile deformation of the cable is linear, the deformation coefficient is denoted as  $k_1$ , the damping inside the cable is denoted as  $k_2$ , and the elongation of the cable and the change rate of the elongation are respectively denoted as  $e_i, \dot{e}_i$   $i = 1, 2, \dots, 8$ . The cable tension is as follows:

$$f_i = \begin{cases} k_1 e_i + k_2 \dot{e}_i & \text{if } e_i > 0 \\ 0 & \text{if } e_i \leq 0 \end{cases} \quad (2)$$

Since the cable can only provide tension, the tension is set to be 0 when the calculated value of tension is less than 0. The initial preload is  $f_{si}$ ,  $i = 1, 2, \dots, 8$ . The elongation of the cable can be calculated as follows.

$$e_i = \Delta l_i - (l_{oi} - l_i) + f_{si} / k_1 \quad (3)$$

Where  $\Delta l_i$  is the length of the driving cable,  $l_i$  is the length of the cable corresponding to the pose, and  $l_{oi}$  is the length of the cable for the initial pose.  $l_i$  and  $l_{oi}$  are solved by the inverse kinematics. The inverse kinematics can be expressed as  $f_{inv}(\mathbf{Pos}) = \mathbf{R}\mathbf{b}_i + \mathbf{t} - \mathbf{c}_i$ .

In this paper, the pose of the mobile platform and the cable tension

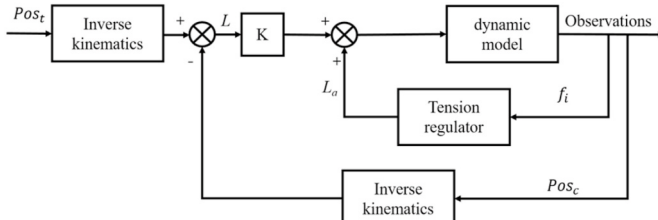


**Fig. 5.** The motion control block diagram of the cable-driven printer.

are used as the feedback variables, and the length of the driving cable is adjusted to reduce the pose error. Fig. 5 shows the motion control strategy of the cable-driven printer. Using the given target pose and the measured current pose  $\mathbf{Pos}_c$ , the driving cable length  $L$  is solved by the inverse kinematics of the cable-driven system  $L = f_{inv}(\mathbf{Pos}_t) - f_{inv}(\mathbf{Pos}_c)$ .  $L$  is multiplied by a scale factor  $K$  and then superimposed with  $L_a$ , and then acts on the dynamic model of the cable-driven printer.  $L_a$  is the cable length adjustment given by a regulator according to the cable tension. The regulator ensures that the cable tension is within a given range  $[f_{min}, f_{max}]$ . Let  $\Delta L_u$  be the cable length adjustment when the tension is less than  $f_{min}$ , and  $\Delta L_u$  is the cable length adjustment when the tension is greater than  $f_{max}$ . The regulation rule in the experiment is: when the pulling force of a cable is greater than  $f_{max}$ , the upper 4 cables release  $\Delta L_u$ ; when the pulling force of a cable is less than  $f_{min}$ , the upper 4 cables are tightened  $\Delta L_u$ .

$$L_a = \begin{cases} -\Delta L_u & \text{if } \forall f_i > f_{max} \\ \Delta L_u & \text{if } \forall f_i \leq f_{min} \end{cases} \quad (4)$$

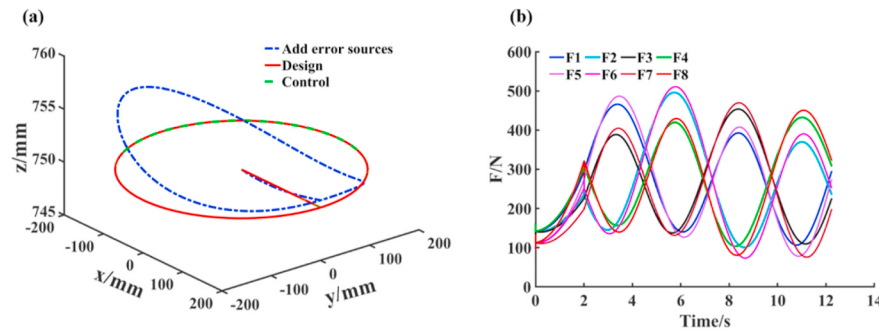
Fig. 6(a) shows the motion simulation trajectory of the cable-driven printer. Added error sources include the deformation coefficient  $k_1$  error, driving cable length error caused by winches and the coordinate error of cable connection points. It can be seen from Fig. 6(a) that the trajectory added error sources is obviously deviated from the design trajectory. The trajectory applied the control strategy almost coincides with the design trajectory. Fig. 6(b) shows that the cable tensions change in a range when the printer is moving with the control strategy, and there is no sharp increase in the tension due to the mutual interference between the cables. The simulation results show that the proposed control strategy is effective for controlling the trajectory accuracy and cable tension of the cable driven printer.

### 4. Reconstruction

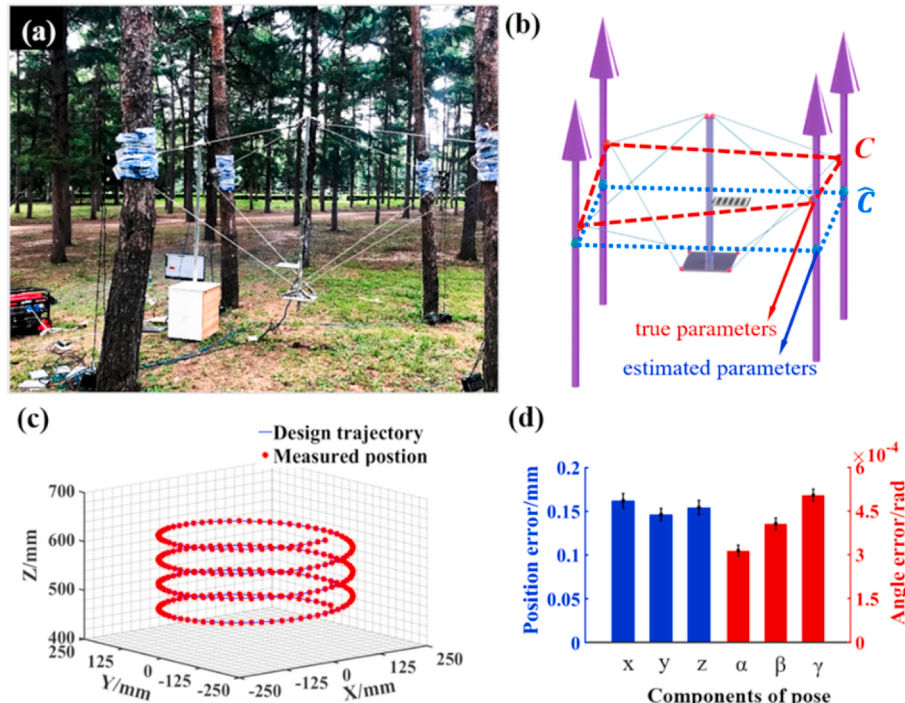
Considering the difficulty and cost of interstellar transportation, the complete frame of the printer in Fig. 3(a) will not be sent to the moon. What is transported to the lunar surface is the frame composed of telescopic rods. When the cable-driven printer is reconstructed in the lunar environment, the rack is randomly placed near the printing location, resulting in unknown reconstruction parameters. For the cable-driven system in this paper, the reconstruction parameters are the coordinates of the intersection points between the cables and the winches, denoted as  $\mathbf{C}$ .  $\mathbf{C}$  is a matrix of  $3 \times 8$ , and each column corresponds to the coordinate of an intersection point. To reflect the randomness of  $\mathbf{C}$ , we selected randomly several trees as the frame to reconstruct the cable-driven printer outdoors.

Fig. 7(a) shows the cable-driven printing system reconstructed on four trees. The distance between the four trees and the fixed height of the winches is unknown. As shown in Fig. 7(b), the intersection point between the cable and the winch is roughly estimated, denoted as  $\widehat{\mathbf{C}}$ . The driving cable length is calculated with  $\widehat{\mathbf{C}}$  and the preset poses. When  $\widehat{\mathbf{C}}$  is quite different from  $\mathbf{C}$ , the cables may be relaxed or over tensioned during operation, which may lead to large trajectory deviation or system damage. The control strategy in Section 3.2 is used to drive the mechanism. Fig. 7(c) shows the measured positions during the operation of the reconstructed cable-driven system. As can be seen from Fig. 7(d), the average position error and the average angle error between measured points and design points is less than 0.2 mm and  $6e^{-4}$  rad, respectively. It shows that the reconstructed system is of good pose accuracy due to the proposed control strategy. The pose error of the system relative to the size of the printed object is entirely acceptable.

The key factor affecting the pose accuracy of the reconstructed system is the sensitivity of the pose of the mobile platform relative to the parameter  $\mathbf{C}$ . In this work, a random deviation is given as  $\mathbf{C}$ . Then the pose deviation is observed to estimate the sensitivity of the pose of the mobile platform relative to  $\mathbf{C}$ .  $\mathbf{C}_r$  is the coordinate of  $\mathbf{C}$  plus random



**Fig. 6.** (a) The motion simulation trajectory of the cable-driven printer. The blue dotted line is the motion trajectory of the cable-driven printer with various error sources. The red line is the designed trajectory. The green dotted line is the trajectory applied the proposed control strategy. (b) The cable tension during the movement of the cable-driven printer with the proposed control strategy. (For interpretation of the references to color in this figure legend, the reader is referred to the Web version of this article.)



**Fig. 7.** Outdoor reconstruction experiment. (a) Reconstructing the system on several trees outside lab. (b)  $\hat{C}$  is the estimated reconstruction parameters and  $C$  is the true reconstruction parameters. (c) Comparison of measured position with designed trajectory. (d) Statistical information on pose error. The abscissa represents the translation and rotation components of the pose.

deviation. In the calculation, 60  $C_r$  were randomly selected. Each  $C_r$  represents the intersection points of the winches and the cables of the reconstructed mechanism. The coordinates of the four selected target points, denoted as  $P$ . According to the dynamic model of the system, the

poses of the mobile platform are calculated, which is denoted as  $P_r$ . In Fig. 8(a), each group of points with the same color corresponds to a  $C_r$ . It can be seen that  $P_r$  has obvious cluster distribution. With the change of reconstruction parameters, the position of printer nozzle fluctuates near

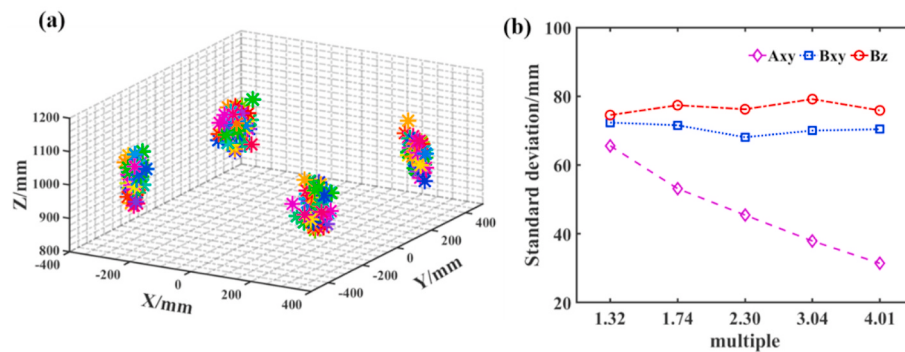


**Fig. 8.** Simulation of sensitivity of the mobile platform relative to selected parameters. (a) Position distribution of the mobile platform corresponding to 60 reconstruction parameters. (b) Change trend of pose deviation sensitivity with selected parameters. The parameters selected are increased proportionally.

the ideal position, which means that the cable-driven printer has good reconstruction characteristics.

The cable-driven system is a miniaturized prototype model. We want to know the pose sensitivity of the real size system relative to the reconstruction parameters. The parameters to be explored are as follows: the  $xy$  coordinate of parameter  $C$ , denoted  $C_{xy}$ ; the  $xy$  coordinate of cable connection points for mobile platforms  $B$ , denoted  $B_{xy}$ ; and the  $z$  coordinates of  $B$ , denoted  $B_z$ . The physical meanings of the selected parameters are as follows: the occupied area of the rack, the size of the rectangular plate of the mobile platform, and the length of the mobile platform rod. The effect of rack height on the sensitivity is not discussed here. This is because changing the rack height is equivalent to moving the workspace up and down. The value of each parameter is magnified by 1.32 times each time.

The standard deviation of the position deviation is selected to describe the corresponding sensitivity.  $C_r$  fluctuates randomly near  $C$ , corresponding to  $P_r$  random fluctuation near  $P$ . The standard deviation of the position deviation of the mobile platform is the statistic of the fluctuation effect, which is used to describe the sensitivity. Although the sensitivity of different pose is different, we are more concerned about the order of magnitude of sensitivity and the trend of sensitivity with each parameter.

**Fig. 8(b)** shows the statistical results of the variation of the standard deviation of the position deviation with each parameter. It can be seen that the range of the rack has a significant influence on the position deviation, while the size of the rectangular plate and the length of the rod have negligible effect on the position deviation. On the premise that the size of the parameter  $C$  fluctuation is constant, the larger the rack area is, the smaller the position deviation is. This is in line with our intuition. It can be imagined that the parameter  $C$  fluctuation can almost be regarded as a point in the space when  $C_{xy}$  has a considerable value, which means that  $C_{xy}$  has no random deviation and  $P_r$  will converge to  $P$ . But it is not that the larger the rack area, the better. With the expansion of the rack area, the tension on the cable will also increase, and the error caused by the cable droop will be more massive. Similarly, although the size of the mobile platform almost does not affect the sensitivity of the position deviation relative to the deviation of  $C$ , it will affect the sensitivity of the position deviation relative to the deviation of  $B$ . In conclusion, for the more extensive size system in the real application, the sensitivity of the position deviation to the reconstruction parameter  $C$  is smaller than that in the paper, and the pose control strategy can effectively reduce the pose error.

## 5. Forming space and printing

Through the previous analysis, we know that the forming space of the cable-driven printer is equivalent to the wrench-feasible workspace

of the mechanism. The solution of the wrench feasible workspace of the cable-driven mechanism with redundant degrees of freedom can be transformed into an optimization problem [13]. The constraint condition of the optimization problem is that the system should satisfy the static equilibrium equation, and the cable tension should be within the given range. The objective function is the maximum value of pulling force in 8 cables. Here, the rotation angle of the mobile platform is set to  $0^\circ$ . The space of  $2000 \text{ mm} \times 2000 \text{ mm} \times 1750 \text{ mm}$  is divided into  $50 \times 50 \times 50$  equal parts. The maximum tensile force that the given cables can withstand is 1000 N. Considering the symmetry,  $1/4$  space is taken as the research object. For each discrete space point, the optimization problem is solved by the interior point method [18,19]. When the optimization problem has no solution, the space point does not belong to the wrench-feasible workspace; when the optimization problem has a solution, it belongs to the wrench-feasible workspace.

**Fig. 9(a)** shows the wrench-feasible workspace of the mechanism in  $1/4$  of the rack space and the maximum tension on the 8 cables at the corresponding space point. The calculation result shows that the wrench-feasible workspace of the cable-driven printer accounts for more than 85% of the total space of the mechanism. In **Fig. 9(a)**, the minimum  $z$  coordinate of the wrench-feasible workspace is about 200 mm instead of 0 mm. In the calculation, the length of the rod of the mobile platform is smaller than the height of the winches. When the  $z$ -coordinate of the actuator is located near 0 mm, all the cables point upward from the actuator to the frame, resulting in that the actuator is not fully constrained. Hence, the spatial points near 0 mm are not in the wrench-feasible workspace. This shows that the pole length of the mobile platform corresponds to the minimum  $z$  coordinate value of the wrench-feasible workspace.

**Fig. 9(b)** and **(d)** show that the forming space of cable-driven printer is almost full of rack space. **Fig. 9(c)** and **(e)** show that the cable tensions on the edge rise sharply as the nozzle approaches the edge of the frame, which limits the forming space of the cable-driven printer. The calculation and the experiments show that the forming space of the proposed cable-driven printer is satisfactory.

We carried out printing experiments to verify the forming ability of the cable-driven system. In the printing experiment, the material is bentonite, and the binder is water. To increase the fluidity of the material during extrusion, the water reducing agent SiKa ViscoCrete-540 P was added to the printing material. The development of lunar cement [20,21] made of lunar soil simulants and additives is not discussed in this paper.

Due to the advantages of sizeable forming space and multi-degree freedom, the cable-driven printing system can be flexibly applied to various printing tasks. It can be used to print the covering layer on the surface of the gasbag as shown in **Fig. 10(a)**, or to print the shell structure as shown in **Fig. 10(c)**. These two types of lunar architecture

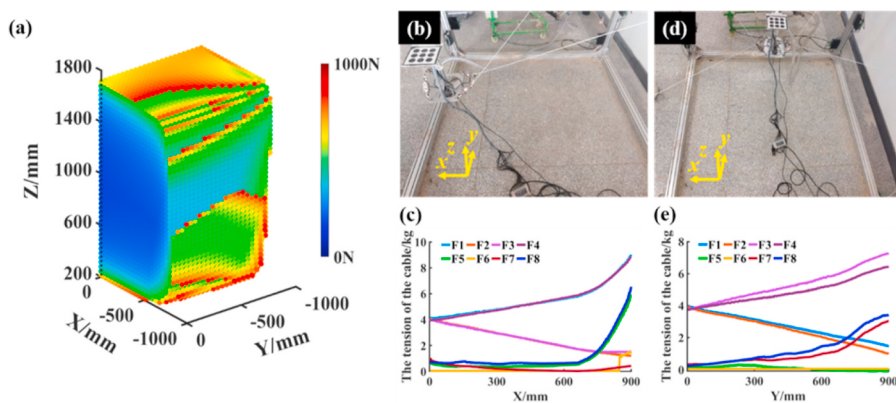


**Fig. 9.** (a) The calculated wrench-feasible workspace of the mechanism in  $1/4$  of the rack space. (b) The experiment of the forming space along the  $x$  direction. (c) The cable tension of printer moving along  $x$  direction. (d) The experiment of the forming space along the  $y$  direction. (e) The cable tension of printer moving along  $y$  direction.

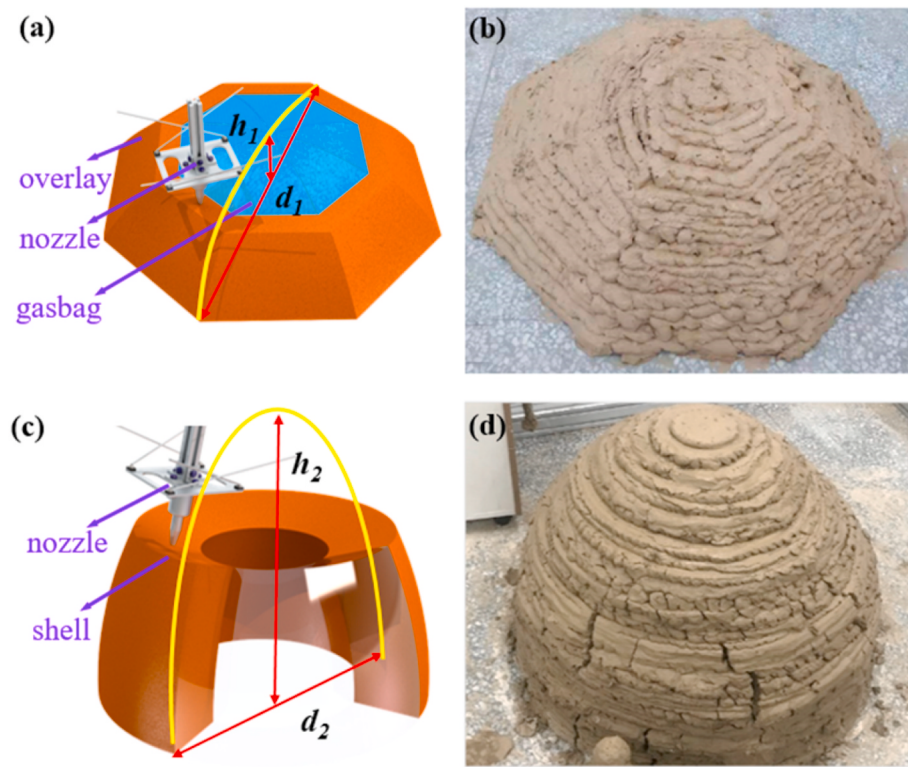


**Fig. 10.** Designed models to be printed along with printed results. (a) The model of the overlay. The brown area in the picture is the part to be printed while the blue area represents the gasbag. (b) The printing result of the overlay. (c) The model of the shell structure, i.e., the middle of the model is empty and however, can be printed without support by tilting the nozzle. (d) The experimental demonstration of the printed shell structure. (For interpretation of the references to color in this figure legend, the reader is referred to the Web version of this article.)

are of great interest for researchers [22–24]. Fig. 10(a) shows a protective layer printed outside the airbag, which is used as a human residence on the lunar surface. Fig. 10(c) is a building printed directly with lunar soil based materials. This building structure is mostly used for equipment protection and storage. These two different structures bring different convenience and difficulties to the printing process: in the actual construction, the airbag shown in Fig. 10(a) will be deformed or can not be accurately placed in the design position, so it is necessary to adjust the printing track in real time, that is, shape-following-printing. However, due to the support of the airbag, the printed object will not collapse during printing. The structure shown in Fig. 10(c) does not need to consider shape-following-printing, but in order to prevent the printing object from collapsing during printing, the building structure cannot have too many suspended parts.

In the experiment, an umbrella was used as the simulation of the gasbag. The bottom of the umbrella is approximately an octagon. The circumscribed circle diameter of the octagon  $d_1$  is 1000 mm. The height of the umbrella  $h_1$  is 240 mm. Fig. 10(b) shows the printing result of the overlay structure. In the experiment, the interference between the moving platform and the covering layer can be avoided effectively by adjusting the pose of the nozzle. Fig. 10(c) shows the designed shell structure. The outline of the structure is obtained by rotating the eggshell curve around the central axis. The wall thickness of the shell is 160 mm, the outer diameter of the bottom  $d_2$  is 800 mm, and the maximum height  $h_2$  is 588 mm. The eggshell curve of the outer contour was equally divided according to the arc length of 11.5 mm, and the inner contour was equally divided according to the arc length of 10 mm. Thus, the height of the outer printing layer is larger than that of the inner printing layer. The printing layer is inclined from the outside to the inside, gradually forming a closed shell. Fig. 10(d) shows the printing result of the shell structure. Due to the large shrinkage of the material after curing, cracks on the printed object shown in Fig. 10(d) are generated. The preliminary printing results show that the designed cable-driven printer has enough stiffness, motion accuracy and motion stability to complete the printing task.

Compared with the current construction equipment, such as gantry

printers [25], arm printers [26], the proposed cable-driven printer has the advantages of light weight, easy to reconstruction. These advantages bring great convenience to the trans planet transportation of the construction equipment. In addition, the proposed cable-driven printer overcomes the shortcoming that the cable of the cable-driven mechanism is easy to interfere with the printed object and has a certain anti-interference ability. Unlike the printing system loaded on the lunar rover, which needs to climb on the air bag during construction, the cable driven printing system can flexibly print the covering layer on a gasbag. With the advantages of multi-degree freedom of the cable-driven system, the printing trajectory can be designed more flexibly to meet more complex lunar architecture. Although extrusion is used in the printing experiment, the cable-driven printing system can flexibly select other printing methods of lunar architecture, such as solar sintering [27], laser sintering [28] etc. Of course, the proposed cable-driven printer also has some shortcomings. The printer needs to be deployed and debugged before printing, so it is not suitable for building lunar facilities that need to move the printer position many times, such as road laying near the lunar base. In addition, the angle range of the mobile platform is small. Therefore, it is difficult for the printer to print the non-uniform structural geometries that requires large angle rotation of the nozzle in printing. Moreover, it is difficult for the printer to print the irregular structures with large cantilever without auxiliary support devices. However, these shortcomings will not become the main limitations in construction.

## 6. Conclusions

This paper presents a cable-driven printer for building lunar architecture. The printer has a large ratio of forming space to mass, which can significantly reduce the cost of trans planet transportation. The designed cable-driven printer does not rely on gravity and effectively avoids interference between the cables and the printed object. The cable-driven printer has a simple structure and good reconstruction performance. The great forming ability of the system is verified by calculation and experiments. These advantages show that the proposed cable-driven

printer has great potential in the construction of lunar buildings in the future.

### Declaration of competing interest

The authors declare that they have no known competing financial interests or personal relationships that could have appeared to influence the work reported in this paper.

### Acknowledgments

This work was partially supported by National Natural Science Foundation of China under Grant Nos. (52005138).

### Appendix A. Supplementary data

Supplementary data to this article can be found online at <https://doi.org/10.1016/j.actaastro.2021.09.034>.

### References

- [1] N. Labeaga-Martínez, M. Sanjurjo-Rivo, J. Díaz-Álvarez, J. Martínez-Frías, Additive manufacturing for a Moon village, *Procedia Manuf.* 13 (2017) 794–801, <https://doi.org/10.1016/j.promfg.2017.09.186>.
- [2] S. Pilehvar, M. Arnhof, R. Pamies, L. Valentini, A.-L. Kjønnsken, Utilization of urea as an accessible superplasticizer on the moon for lunar geopolymers mixtures, *J. Clean. Prod.* 247 (2020) 119177, <https://doi.org/10.1016/j.jclepro.2019.119177>.
- [3] G.H. Just, K. Smith, K.H. Joy, M.J. Roy, Parametric review of existing regolith excavation techniques for lunar in situ Resource Utilisation (ISRU) and recommendations for future excavation experiments, *Planet. Space Sci.* 180 (2020) 104746, <https://doi.org/10.1016/j.pss.2019.104746>.
- [4] A. Ellery, Sustainable in-situ resource utilization on the moon, *Planet. Space Sci.* 184 (2020) 104870, <https://doi.org/10.1016/j.pss.2020.104870>.
- [5] K. Hadler, D.J.P. Martin, J. Carpenter, J.J. Cilliers, A. Morse, S. Starr, J.N. Rasera, K. Seweryn, P. Reiss, A. Meurisse, A universal framework for space resource utilisation (SRU), *planet. Space Sci.* 182 (2020) 104811, <https://doi.org/10.1016/j.pss.2019.104811>.
- [6] G. Cesaretti, E. Dini, X. De Kestelier, V. Colla, L. Pambagian, Building components for an outpost on the Lunar soil by means of a novel 3D printing technology, *Acta Astronaut.* 93 (2014) 430–450, <https://doi.org/10.1016/j.actaastro.2013.07.034>.
- [7] X. Zhang, M. Li, J.H. Lim, Y. Weng, Y.W.D. Tay, H. Pham, Q.-C. Pham, Large-scale 3D printing by a team of mobile robots, *Autom. ConStruct.* 95 (2018) 98–106, <https://doi.org/10.1016/j.autcon.2018.08.004>.
- [8] C. Zhou, R. Chen, J. Xu, L. Ding, H. Luo, J. Fan, E.J. Chen, L. Cai, B. Tang, In-situ construction method for lunar habitation: Chinese Super Mason, *Autom. ConStruct.* 104 (2019) 66–79, <https://doi.org/10.1016/j.autcon.2019.03.024>.
- [9] S. Qian, B. Zi, W.-W. Shang, Q.-S. Xu, A review on cable-driven parallel robots, *Chin. J. Mech. Eng.* 31 (2018) 1–11, <https://doi.org/10.1186/s10033-018-0267-9>.
- [10] X. Tang, An overview of the development for cable-driven parallel manipulator, *Adv. Mech. Eng.* 6 (2014) 823028, <https://doi.org/10.1155/2014/823028>.
- [11] P. Bosscher, R.L. Williams II, L.S. Bryson, D. Castro-Lacouture, Cable-suspended robotic contour crafting system, *Autom. ConStruct.* 17 (2007) 45–55, <https://doi.org/10.1016/j.autcon.2007.02.011>.
- [12] E. Barnett, C. Gosselin, Large-scale 3D printing with a cable-suspended robot, *Addit. Man. (Lond.)* 7 (2015) 27–44, <https://doi.org/10.1016/j.addma.2015.05.001>.
- [13] T. Bruckmann, A. Pott, *Cable-driven Parallel Robots*, Springer, 2012, <https://doi.org/10.1007/978-3-319-09489-2>.
- [14] C. Gao, N. Ahuja, Single camera stereo using planar parallel plate, *Proc. 17th Int. Conf. Pattern Recognition* (2004) 108–111, <https://doi.org/10.1109/ICPR.2004.133717>. ICPR 2004., IEEE, 2004.
- [15] W. Lovegrove, B. Brame, Single-camera stereo vision for obstacle detection in mobile robots, *Intell. Robot. Comput. Vis. XXV Algorithms, Tech. Act. Vis.*, International Society for Optics and Photonics, 2007, p. 676407, <https://doi.org/10.1117/12.732651>.
- [16] L. Duvieubourg, S. Ambellouis, S. Lefebvre, F. Cabestaing, Obstacle detection using a single camera stereo sensor, *2007 Third Int. IEEE Conf. Signal-Image Technol. Internet-Based Syst.* (2007) 979–986, <https://doi.org/10.1109/SITIS.2007.26>. IEEE.
- [17] X.-S. Gao, X.-R. Hou, J. Tang, H.-F. Cheng, Complete solution classification for the perspective-three-point problem, *IEEE Trans. Pattern Anal. Mach. Intell.* 25 (2003) 930–943, <https://doi.org/10.1109/TPAMI.2003.1217599>.
- [18] R.A. Waltz, J.L. Morales, J. Nocedal, D. Orban, An interior algorithm for nonlinear optimization that combines line search and trust region steps, *Math. Program.* 107 (2006) 391–408, <https://doi.org/10.1007/s10107-004-0560-5>.
- [19] R.H. Byrd, J.C. Gilbert, J. Nocedal, A trust region method based on interior point techniques for nonlinear programming, *Math. Program.* 89 (2000) 149–185, <https://doi.org/10.1007/PL00011391>.
- [20] J.M. Neves, S. Ramanathan, P. Suraneni, R. Grugel, A. Radlińska, Characterization, mechanical properties, and microstructural development of lunar regolith simulant-portland cement blended mixtures, *Construct. Build. Mater.* 258 (2020) 120315, <https://doi.org/10.1016/j.conbuildmat.2020.120315>.
- [21] M. Isachenkov, S. Chugunov, I. Akhatov, I. Shishkovsk\_Y, Regolith-based additive manufacturing for sustainable development of lunar infrastructure – an overview, *Acta Astronaut.* 180 (2021), <https://doi.org/10.1016/j.actaastro.2021.01.005>.
- [22] N. Kalapodis, G. Kampas, O.-J. Ktenidou, A review towards the design of extraterrestrial structures: from regolith to human outposts, *Acta Astronaut.* 175 (2020) 540–569, <https://doi.org/10.1016/j.actaastro.2020.05.038>.
- [23] F. Ruess, J. Schaenzlin, H. Benaroya, Structural design of a lunar habitat, *J. Aero. Eng.* 19 (2006) 133–157, [https://doi.org/10.1061/\(ASCE\)0893-1321,2006193\(133](https://doi.org/10.1061/(ASCE)0893-1321,2006193(133).
- [24] R.B. Malla, D. Chaudhuri, Analysis of a 3D frame—membrane structure for lunar base, *Earth Sp. 2006 Eng. Constr. Oper. Challenging Environ.* (2006) 1–8, [https://doi.org/10.1061/40830\(188\)61](https://doi.org/10.1061/40830(188)61).
- [25] R.J.M. Wolfs, F.P. Bos, E.C.F. van Strien, T.A.M. Salet, A real-time height measurement and feedback system for 3D concrete printing, *High Tech Concr. Where Technol. Eng. Meet.*, Springer, 2018, pp. 2474–2483. [https://link.springer.com/chapter/10.1007%2F978-3-319-59471-2\\_282](https://link.springer.com/chapter/10.1007%2F978-3-319-59471-2_282).
- [26] S.J. Keating, J.C. Leland, L. Cai, N. Oxman, Toward site-specific and self-sufficient robotic fabrication on architectural scales, *Sci. Robot.* 2 (2017), <https://doi.org/10.1126/scirobotics.aam8986>.
- [27] M. Fateri, A. Meurisse, M. Sperl, D. Urbina, H.K. Madakashira, S. Govindaraj, J. Gancet, B. Imhof, W. Hoheneder, R. Waclavicek, Solar sintering for lunar additive manufacturing, *J. Aero. Eng.* 32 (2019) 4019101, [https://doi.org/10.1061/\(ASCE\)AS.1943-5525.0001093](https://doi.org/10.1061/(ASCE)AS.1943-5525.0001093).
- [28] L. Caprio, A.G. Demir, B. Previtali, B.M. Colosimo, Determining the feasible conditions for processing lunar regolith simulant via laser powder bed fusion, *Addit. Manuf.* 32 (2020) 101029, <https://doi.org/10.1016/j.addma.2019.101029>.